OPEN ACCESS
IOP Publishing | International Atomic Energy Agency
Nuclear Fusion
Nucl. Fusion **66** (2026) 116005 (17pp)
https://doi.org/10.1088/1741-4326/ae63e1

Overview of the MAST Upgrade physics programme: testing novel concepts at low aspect ratio to inform future devices

J.R. Harrison[1,*], A. Aboutaleb[2], M. Aljunid[1], S.Y. Allan[1], R. Allan[1], A. Alli[1], H. Anand[3], Y. Andrew[4], L.C. Appel[1], A. Ash[1], J. Ashton[1], F. Auriemma[5], O. Bachmann[1], S. Bakes[1], P. Balazs[6], O. Bardsley[1], M. Barnes[7], B. Barrett[1], D. Baver[8], C. Beckley[1], J. Bennett[1], J. Bentley[1], J. Berkery[9], M. Bernert[10], N. Bertelli[9], P. Bilkova[11], S. Blackmore[1], A. Bock[10], W. Boeglin[2], P. Bohm[11], J. Booth[1], A. Bosnjak[1], C. Bowman[1], J. Bradley[12], L. Bramucci[13], D. Brida[10], M. Brix[1], P.K. Browning[14], D. Brunetti[1], P. Bryant[12], J. Bryant[12], J. Buchanan[1], M. Bull[1], M. Bulman[1], N. Bulmer[1], D. Burke[1], P. Cahill[1], P. Cano-Megías[15], M. Carpita[16], A. Carruthers[1], L. Casali[17], A. Cassidy[1], F. Causa[18], M. Cecconello[19,20], A. Celora[21], M. Cha[22], B. Chamberlain[1], B. Chapman[1], B. Chapman-Oplopoiou[1], R. Chazal[1], X. Chen[3], J. Clark[9], M. Clark[1], T. Clayton[1], K. Collie[1], D. Collishaw-Schepman[1], J.W. Connor[1], M. Coy[1], S. Cramp[1], N. Crocker[23], D. Cruse[1], G. Cunningham[1], M. Czarski[24], I. Cziegler[25], Y. Damizia[12,26], P. Davies[1], K. Davies[1], I. Day[1], E. Delabie[27], G.L. Derks[28,29], S. Dixon[1], J. Dobrashian[1], M. Dreval[30], X. Du[3], H. Dudding[1], D. Dunai[6], M. Dunne[10], F. Ebrahimi[9], J. Edmond[1], J. Edwards[1], H. El-Haroun[1], S. Elmore[1], Y. Enters[25], M. Faitsch[10], F. Federici[27], N. Fedorczak[31], F. Felici[16], N. Ferraro[9], A.R. Field[1], P. Figueiredo[32], I. FitzGerald[1], M. Fitzgerald[1], R. Fitzpatrick[33], C. Fitzpatrick[9], S. Frankel[1], L. Frassinetti[34], D. Frattolillo[35], S. Freethy[1], W. Fuller[36], R. Futtersack[1], S. Gabriellini[1], K. Gage[23], J. Galdon[15], J. Galdon-Quiroga[15], M. Gambrioli[13], C. Garner[1], L. Garzotti[1], T.E. Gheorghiu[1,25], K.J. Gibson[25], C. Gibson[1], E. Giovannozzi[37], C. Giroud[1], J. Goatley[1], A. Goodyear[1], M. Gorelenkova[9], S. Gosden[1], G. Grassler[38], J.P. Graves[25,39], D. Greenhouse[25,40], R. Griffiths[1], V.H. Hall-Chen[41], C.J. Ham[1], E. Harrington[1], R. Harrison[1], A. Haupt[1], J. Hawes[1], S. Hegedus[6], S.S. Henderson[1], C. Heo[22], C. Hickling[1], M. Hill[1], B. Hnat[42], C. Hogben[1], B. Honey[1], L. Howlett[1], Z. Huang[1], A. Hudoba[1], J. Hughes[43], R. Hussain[1], K. Imada[3,25], P. Ivanov[1], A. Jackson[2], P. Jacquet[1], F. Jaulmes[44], P. Jepson[1], T. Jones[1], P. Jones[1], M. Juvonen[1], V. Kachkanov[1], B. Kandan[1], I. Katramados[1], S. Kaye[9], Y.O. Kazakov[45], D. Keeling[1], D. Kennedy[1], A. Kenny[1], H-T. Kim[1], D. King[1], R. King[1], A. King[1], V. Kiptily[1], A. Kirjasuo[46], A. Kirk[1], A. Kit[46], A. Kleiner[9], M. Knolker[3], S. Kobussen[32], M. Kochan[1], L. Kogan[1], B. Kool[28,29], D. Kos[1], M. Kotschenreuther[33,47], M. Lampert[9], A. Lawson[1], K. Lawson[1], K.-W. Lee[17], G. Lee[1], J. Lee[22], M. Lees[1], S. Leigh[1], A.W. Leonard[3], G. Liddiard[1], B. Lipschultz[25], E. Litherland-Smith[1], Y.Q. Liu[3], B.A. Lomanowski[27], J. Lombardo[13], N. Lonigro[1,25], J. Lore[27], J. Lovell[27], R. Lucock[1], T. Luong[23], A. Lvovskiy[3], J. Macdonald[1], T. Macwan[48], S. Mahajan[33], F. Maiden[25], R. Maingi[9], C. Man-Friel[1], F. Mansfield[1], M. Markl[38], S. Marsden[1], R. Martin[1], R. Mathew[1], R. Maurizio[3], U. Mazzarese[1], S. Mazzi[16],

[*] Author to whom any correspondence should be addressed.

R. McAdams[1], G. McArdle[1], J. McBride[1], K. McClements[1], J. McClenaghan[3], D. McConville[1], K. McKay[12], C. McKnight[1], P. McKnight[1], A. McLean[48], B.F. McMillan[42], A. McShee[1], J. Measures[1], N. Mehay[1], S. Menmuir[1], H.F. Meyer[1], C.A. Michael[23], F. Militello[1], I.G. Miron[49], R. Mishra[24], J. Mitchell[1], D. Moiraf[31], P. Monaghan[1], R. Mooney[1], N. Mooring[1], R. Morales Gomes[1], D. Morbey[1], S. Mordijck[26], C. Morgan[1], J. Morris[1], D. Moulton[1], S. Munaretto[9], A. Munasinghe[1], A. Muraro[18], O. Myatra[1], Y.-S. Na[22], T.F. Neiser[3], A.O. Nelson[50], S.L. Newton[1], M. Nicassio[1], M.G. O'Mullane[51], C. Olde[1], H.J. Oliver[1], P. Ollus[52], J. Omotani[1], M. Ono[9], F.P. Orsitto[37], R. Osawa[1], N. Osborne[1,12], T. Osborne[3], R. Otin[1], E. Ozturk[26,53], F. Palermo[1], A. Pankin[9], I. Paradela Pérez[27], J. Parisi[9,54], E. Parr[1], B. Parry[1], B.S. Patel[1], E. Pawelec[55], D. Payne[1], C. Paz-Soldan[50], A. Phelps[51], L. Piron[5], C. Piron[56], G. Pokol[6], R. Preece[1], M. Price[1], B. Pritchard[25], R. Proudfoot[1], G. Pucella[56], T. Pumfrett[1], D.-Y. Pyo[22], H. Reimerdes[16], T. Rhodes[23], E. Ribeiro[1], D. Rigamonti[57], J. Riquezes[50], J.F. Rivero-Rodriguez[15], J. Roberts[1], M. Robson[1], K. Ronald[51], E. Rose[1], D. Ryan[1], P. Ryan[1], S. Saarelma[1], S. Sabbagh[50], A. Salmi[46], R. Sarwar[1], P. Saunders[1], O. Sauter[16], R. Scannell[1], R. Sealey[1], R. Seath[1], S. Sharapov[1], R. Sharma[1], H. Sheikh[1], S. Shiraiwa[9], B. Sieglin[10], S.A. Silburn[1], M. Simmonds[1], J. Simpson[1], A. Sladkomedova[58], J. Smith[1], P. Smith[1], M. Sos[11], V.A. Soukhanovskii[48], D. Speirs[51], C. Srinivasan[1], G. Staebler[27], R. Stephen[1], P. Stevenson[1], J. Stobbs[10], C. Stroud[1], H. Sun[16], H. Sun[1], G. Szepesi[1], D.M. Takács[6], T. Tala[46], C. Tame[1], C. Theiler[16], B. Thomas[1], S. Thomas[1], S. Thomas[43], N. Thomas-Davies[1], A.J. Thornton[1], A. Tilley[1], I. Tirkova[1], M. Tobin[50], E. Tomasina[13], A. Tonel[13], P. Tonner[1], A. Tookey[1], G. Tvalashvili[1], M. Vallar[16], M. Valovic[1], R.G.L. Vann[25], L. Velarde[15], L. Velarde[15], K. Verhaegh[29], E. Viezzer[15], C. Vincent[1], M. Walsh[1], T. Walsh[1], M. Warr[1], S. Wiesen[28], T.A. Wijkamp[28,29], D. Wilkins[1], J. Willis[1], T. Wilson[1], H.R. Wilson[1], N. Winston[1], G. Withenshaw[1], H. Wong[23], M. Wood[1], R. Worrall[1], Q. Xia[1], G. Xia[1], L. Xiang[1], G. Xiang[1], T. Xu[1], J.H. Yu[3], V. Zamkovska[50], M. Zerbini[37], V.K. Zotta[59], M. Zurita[16] and L.E. di Grazia[35]

[1] UKAEA (United Kingdom Atomic Energy Authority), Culham Campus, Abingdon, Oxfordshire OX14 3DB, United Kingdom of Great Britain and Northern Ireland
[2] Department of Physics, Florida International University, 11200 SW, Miami, FL 33199, United States of America
[3] General Atomics, PO Box 85608, San Diego, CA 92186-5608, United States of America
[4] Blackett Laboratory, Imperial College London, London SW7 2BW, United Kingdom of Great Britain and Northern Ireland
[5] Consorzio RFX (CNR, ENEA, INFN, Università di Padova, Acciaierie Venete SpA), Corso Stati Uniti 4, Padova 35127, Italy
[6] Centre for Energy Research, POB 49, Budapest H-1525, Hungary
[7] Rudolf Peierls Centre for Theoretical Physics, University of Oxford, Oxford OX1 3NP, United Kingdom of Great Britain and Northern Ireland
[8] Astrodel
[9] Princeton Plasma Physics Laboratory, Princeton, NJ, United States of America
[10] Max-Planck-Institute fur Plasmaphysik, 85748 Garching, Germany
[11] Institute of Plasma Physics of the CAS, Za Slovankou 1782/3, Praha 8 182 00, Czech Republic
[12] Department of Electrical Engineering and Electronics, University of Liverpool, Brownlow Hill, Liverpool L69 3GJ, United Kingdom of Great Britain and Northern Ireland
[13] Consorzio RFX (CNR, ENEA, INFN, University of Padova, Acciaierie Venete SpA), C.so Stati Uniti 4, Padova 35127, Italy
[14] Department of Physics and Astronomy, University of Manchester, Oxford Road, Manchester M13 9PL, United Kingdom of Great Britain and Northern Ireland
[15] Departamento de Física Atómica, Molecular y Nuclear, Universidad de Sevilla, Sevilla, Spain
[16] École Polytechnique Fédérale de Lausanne (EPFL), Swiss Plasma Center (SPC), CH-1015 Lausanne, Switzerland
[17] University of Tennessee, Knoxville, Knoxville, TN 37996, United States of America
[18] Institute for Plasma Science and Technology, CNR, via R. Cozzi 53, Milano 20125, Italy

[19] Department of Physics, Durham University, Durham DH1 3LE, United Kingdom of Great Britain and Northern Ireland
[20] Department of Physics and Astronomy, Uppsala University, Uppsala SE-75105, Sweden
[21] University of Milano-Bicocca, Piazza della Scienza 3, Milano 20126, Italy
[22] Department of Nuclear Engineering, Seoul National University, Seoul, Republic Of Korea
[23] Physics and Astronomy Department, University of California, Los Angeles, CA 90098, United States of America
[24] Institute of Plasma Physics and Laser Microfusion, Hery 23 01-497 Warsaw, Poland
[25] York Plasma Institute, Department of Physics, University of York, Heslington, York YO10 5DD, United Kingdom of Great Britain and Northern Ireland
[26] Department of Computer Science, College of William & Mary, Williamsburg, VA, United States of America
[27] Oak Ridge National Laboratory, Oak Ridge, TN 37831, United States of America
[28] Dutch Institute for Fundamental Energy Research DIFFER, Eindhoven, Netherlands
[29] Eindhoven University of Technology, Eindhoven, Netherlands
[30] National Science Center 'Kharkov Institute of Physics and Technology', Akademichna 1, Kharkiv 61108, Ukraine
[31] CEA, IRFM, Saint-Paul-lez-Durance F-13108, France
[32] Dutch Institute for Fundamental Energy Research, P.O. Box 6336, HH Eindhoven 5600, Netherlands
[33] Institute for Fusion Studies, The University of Texas at Austin, Austin, TX, United States of America
[34] Division of Fusion Plasma Physics, KTH Royal Institute of Technology, Stockholm SE-100 44, Sweden
[35] Consorzio CREATE, Via Claudio 21, Napoli 80125, Italy
[36] Department of Physics, University of Warwick, Coventry CV4 7AL, United Kingdom of Great Britain and Northern Ireland
[37] ENEA, NUC, Centro Ricerche Frascati, Via E. Fermi 45, Frascati (Roma) 00044, Italy
[38] Graz University of Technology, Petersgasse 16 8010 Graz, Austria
[39] Ecole Polytechnique Fédérale de Lausanne (EPFL), Swiss Plasma Center (SPC), Lausanne CH-1015, Switzerland
[40] digiLab, The Quay, Exeter EX2 4AN, United Kingdom of Great Britain and Northern Ireland
[41] Institute of High Performance Computing A*STAR, Singapore
[42] Department of Physics, University of Warwick, Coventry CV4 7AL, United Kingdom
[43] Plasma Science and Fusion Center, Massachusetts Institute of Technology, Cambridge, MA 02139, United States of America
[44] Institute of Plasma Physics of the CAS, Za Slovankou 1782/3, Prague 8 182 00, Czech Republic
[45] Laboratory for Plasma Physics, LPP-ERM/KMS, TEC Partner, Brussels, Belgium
[46] VTT Technical Research Centre of Finland, PO Box 1000, FIN-02044 VTT, Finland
[47] ExoFusion
[48] Lawrence Livermore National Laboratory, Livermore, CA, United States of America
[49] The National Institute for Laser, Plasma and Radiation Physics, Magurele, Bucharest, Romania
[50] Department of Applied Physics and Applied Mathematics, Columbia University, New York, NY, United States of America
[51] Department of Physics, SUPA, University of Strathclyde, Glasgow, Scotland, United Kingdom of Great Britain and Northern Ireland
[52] Department of Applied Physics, Aalto University, PO Box 11100, 00076 Aalto, Finland
[53] Department of Computing, Imperial College, Prince Consort Road, London SW7 2BZ, United Kingdom of Great Britain and Northern Ireland
[54] Marathon Fusion, 150 Mississippi, San Francisco, CA 94107, United States of America
[55] Institute of Physics, University of Opole, Oleska 48 45-052 Opole, Poland
[56] ENEA, Fusion and Nuclear Safety Department, C. R. Frascati, Via E. Fermi 45, Frascati 00044, Roma, Italy
[57] Polytechnique de Paris, Palaiseau, France
[58] Tokamak Energy Ltd., 173 Brook Drive, Milton Park, Oxfordshire OX14 4SD, United Kingdom
[59] Dipartimento di Ingegneria Astronautica, Elettrica ed Energetica, SAPIENZA Università di Roma, Via Eudossiana 18, Roma 00184, Italy

E-mail: James.Harrison@ukaea.uk

Received 6 January 2026, revised 16 March 2026
Accepted for publication 23 April 2026
Published 18 May 2026

Abstract

The research programme performed on the Mega Amp Spherical Tokamak (MAST) Upgrade experiment has made significant advances in developing the physics understanding of low

aspect ratio tokamaks in support of the operation of ITER and design of fusion powerplants. High performance plasma scenarios have been developed to facilitate a broad programme of experiments, in which confinement is constrained by the presence of $m/n = 2/1$ modes that cause substantial losses of fast ions. The onset of these modes coincides with the $q = 2$ surface residing in a local minimum in the toroidal current density profile. The maximum electron temperature at the pedestal top, $T_{e,ped}$ is limited with gas fuelling to $\sim$350 eV to maintain regular ELMs; higher $T_{e,ped}$ results in a transition to a non-stationary ELM-free regime. The operational space of spherical tokamaks has been expanded into small and ELM-free regimes. Strong shaping of the last closed flux surface can induce a transition from large to small ELMs, and ELM suppression with resonant magnetic perturbations has been observed for the first time in a low aspect ratio tokamak. Negative triangularity shaping has induced a transition from ELMy H-mode to a high-performance L-mode regime for the first time in a low aspect ratio tokamak. In studies of fast ion confinement, losses of fast particles due to Global Alfvén Eigenmodes have been identified. Interactions between fast ions generated by off-axis neutral beam injection and thermal neutrals can result in significant losses of fast ions. Experiments with on- and off-axis neutral beam injection exhibit a flux pumping mechanism, where the central safety factor is held to $\sim$1 in the absence of sawteeth. In studies of pedestal physics, it has been found that elevated main chamber neutral pressures result in an increase in the electron density and reduction in the temperature at the pedestal top. Advances in understanding plasma exhaust include the integration of a high-performance plasma core with detached outer divertors in the *X*-point target configuration. A newly commissioned lower divertor cryopump reduces the lower divertor neutral pressure by up to 50%, with minimal effect on the main chamber or upper divertor. New measurements and SOLPS-ITER simulations emphasise the importance of plasma–neutral interactions on divertor detachment in the conditions accessible in experiments. Real-time control of the ionisation front location in both divertor chambers independently has been demonstrated in double null experiments, enabled by the tightly baffled divertor chambers.

Keywords: MAST Upgrade, overview, spherical tokamak

(Some figures may appear in colour only in the online journal)

1. Introduction

Mega Amp Spherical Tokamak (MAST) Upgrade [1] (shown schematically in figure 1) is a low aspect ratio tokamak (major radius/minor radius $(R/a) = 0.85/0.65 \sim 1.3$, plasma current $(I_p) \leqslant 2.0$ MA, toroidal field on axis $(B_\varphi) \leqslant 0.8$ T, pulse length < 5 s) and one of the largest spherical tokamaks (STs) worldwide, together with NSTX-U [2]. Key features include 22 poloidal field coils to provide considerable flexibility to independently vary the shape of the plasma core and divertors within tightly baffled chambers. Coils to produce non-axisymmetric fields for control of edge localised modes (ELMs) with resonant magnetic perturbations (RMPs) and to correct for intrinsic error fields are available, with two rows of in-vessel coils (four equally spaced toroidally above the mid-plane, eight below) and two pairs of ex-vessel coils respectively. On- and off-axis neutral beam injectors (NBIs) with tangency positions (*R, Z*) of (0.71 m, 0.0 m) and (0.8 m, 0.65 m) respectively, are external sources of heat and momentum to the plasma and enable studies of the confinement of super Alfvénic fast ions that more closely mimics the confinement of fusion products. An extensive suite of diagnostics is available to support a broad and deep physics programme in these important physics issues for the operation of ITER and the design of future power plants including DEMO [3] and STEP [4].

Recent physics results from MAST Upgrade make significant and unique advances in understanding key physics issues governing the operation of ITER and the design of future fusion power plants. The operating space has expanded considerably thanks to new capabilities including an active lower divertor cryopump to control the neutral pressure and sophisticated real-time equilibrium shape control to reach higher elongation ($\kappa \sim 1.8 \rightarrow 2.5$) and a larger range of triangularity ($\delta \sim -0.15 \rightarrow 0.5$), reaching negative triangularity for the first time in a ST. Operation with Super-*X* divertor configurations in the attached regime has been achieved with the cryopumped divertor, enabling studies of detachment onset. The plasma conditions in the divertors and main chamber can be effectively decoupled, due to the tightly baffled divertor chambers, which is rarely observed in current devices and enables pioneering studies of core-edge-divertor integration. Recent results from MAST Upgrade are presented, emphasising results that develop the physics basis for STs and future high beta devices.

2. Integrated plasma scenarios

The development of high-performance plasma scenarios50796, 504 provides the foundations for the wider research programme. The integrated scenarios programme has two main goals: to develop reproducible scenarios that

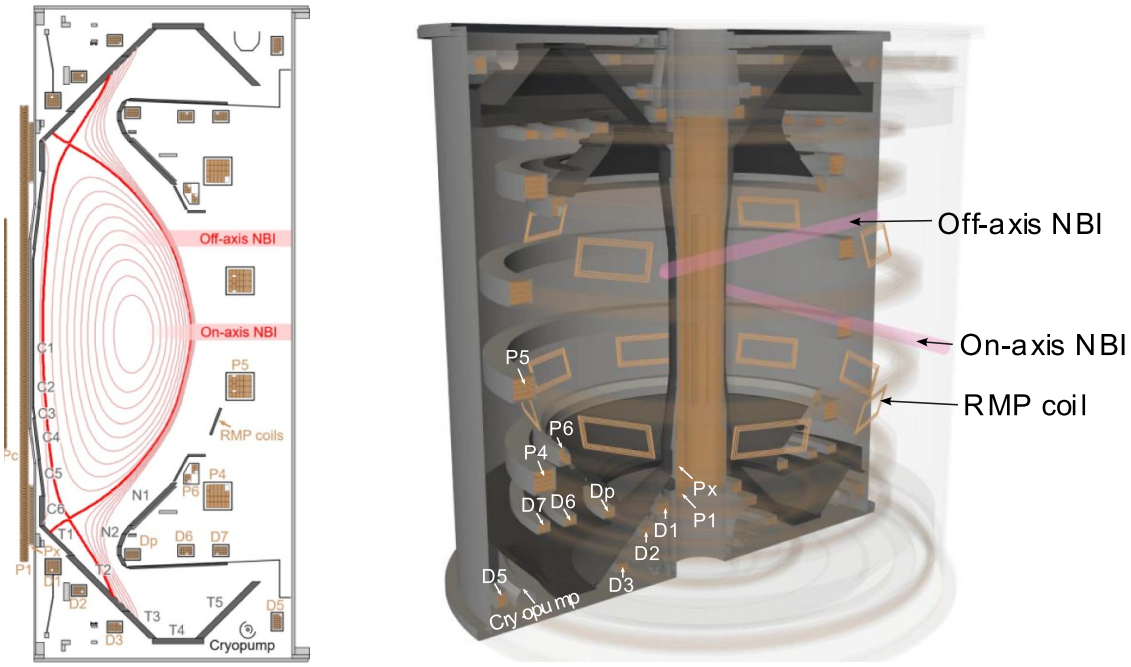

Figure 1. Left—poloidal cross-section of MAST Upgrade. The central solenoid (P1), poloidal field coils to shape the plasma core (P4, P5), control the plasma vertical position (P6), inner gap (Pc, Px) and the divertor configuration (D1–D7) and graphite tiles lining the centre column (C1–C6), main divertor tiles (T1–T5) and on the divertor nose (N1–N2) are labelled. The components in the lower half of the machine are identical to their counterparts in the upper half. Right—3D representation of MAST Upgrade with the neutral beams, RMP coils and poloidal field coils labelled.

maximise confinement of thermal and fast particles and magnetohydrodynamic (MHD) stability, and to develop strongly shaped, highly elongated plasmas with high central safety factor (q_0) to explore stability and confinement with more reactor-relevant q profiles (e.g. compared with STEP [4] and other ST-based concepts [5]) and shape of the plasma boundary. In both scenarios, significant effort was dedicated to optimising the early ramp-up phase to tailor the equilibrium q profile. Real-time control of the line-integrated density at the mid-plane has been developed for use in L-mode plasma scenarios. The feedback controller uses real-time measurements from an interferometer at the midplane and a proportional integral controller developed using system identification experiments to ascertain the response of the plasma density to time-varying gas fuelling [6].

In the high confinement scenario, the I_p ramp-up phase was developed with the CREATE-ILC (Iterative Learning Control) tool [7] with the currents in the poloidal field coils and central solenoid placed under feedforward control, transitioning to feedback in the plasma current flat-top phase. The target flat-top plasma current and toroidal field on axis were 0.75 MA and 0.65 T respectively to achieve conditions optimal for studies of plasma exhaust [8] and more favourable MHD stability. The ramp-up phase is shown to be very robust to changes in vacuum conditions and the timing of neutral beam injection (see figure 2).

The conditions required for reliable plasma breakdown were guided by the DYON code [9] that has been successfully tested against experiments performed on MAST and MAST Upgrade. Internal reconnection events, disruptive events often triggered when the equilibrium q profile exhibits strong reverse shear, have been avoided despite having a relatively high plasma current ramp rate, up to ~6 MA s^{-1}. Equilibrium shape controllers in the flat-top phase were developed using the TokSys framework [10, 11] to enable fine control of the shape of the plasma boundary and divertor configuration independently. Careful tailoring of the shape of the last closed flux surface and fuelling of the plasma core are required in H-mode to achieve steady type-I ELMs throughout the flat-top phase. High triangularity and/or squareness can result in a transition to a type-II ELMing regime and low fuelling can result in high pedestal temperatures ($T_{e,ped} > 350$ eV) that stimulates a transition to an ELM-free regime (see figure 3). This transition from ELMing to ELM-free pedestals is consistent with toroidal mode number $(n) = \infty$ ballooning stability calculations showing that the edge of the plasma is unstable to these modes, which are commonly used as a proxy for kinetic ballooning modes (KBMs, e.g. [12].). These KBMs can increase radial transport across the pedestal to limit the pedestal pressure gradient, thus avoiding the triggering of ELMs. The thermal and fast ion confinement is limited by $m/n = 2/1$ (where m is the poloidal mode number) tearing modes that are ubiquitous in neutral beam heated H-modes on MAST Upgrade and are described in more detail in section 5.

A plasma scenario with high central safety factor (q_0) was developed in parallel with its high confinement counterpart described earlier in this section, sharing developments that would benefit the other, as both scenarios have identical flat-top plasma current and toroidal field on axis. Consequently, the operating space of MAST Upgrade, illustrated in figure 4,

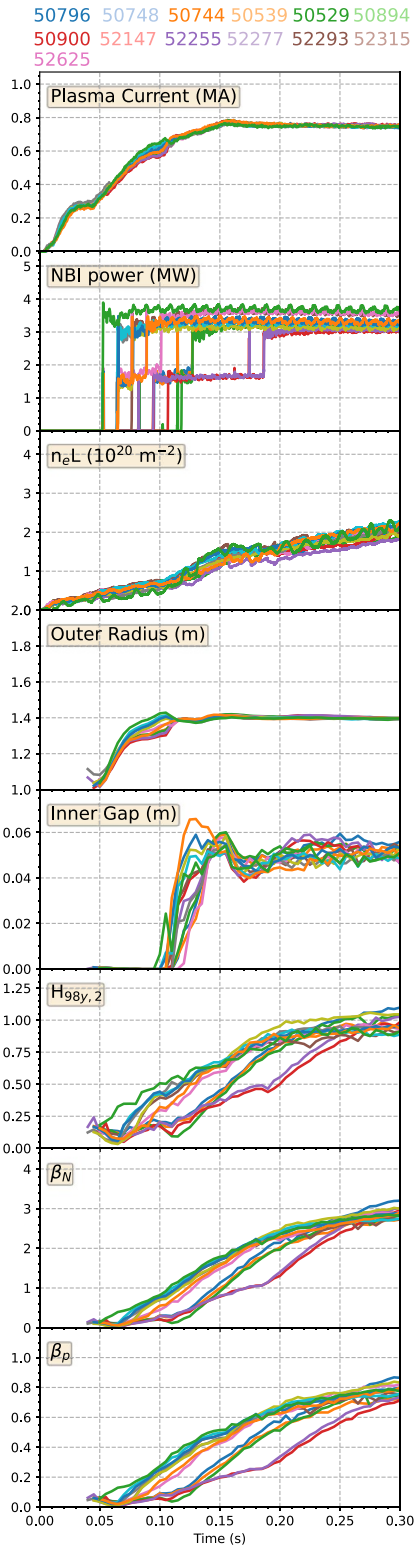

Figure 2. Sensitivity of the ramp-up phase of the high confinement scenario to variation in neutral beam timing, showing, starting from the upper plot, the plasma current evolution and inner and outer radii, normalised energy confinement, normalised β and poloidal β.

expanded towards higher elongation (κ, defined as the ratio of the vertical and radial extent of the last closed flux surface). The plasma breakdown phase is performed at lower solenoid premagnetisation current to enable the formation of

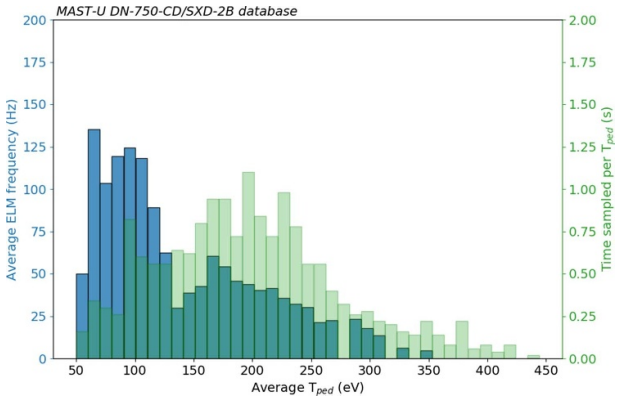

Figure 3. Dependence of ELM frequency on the electron temperature at the top of the pedestal.

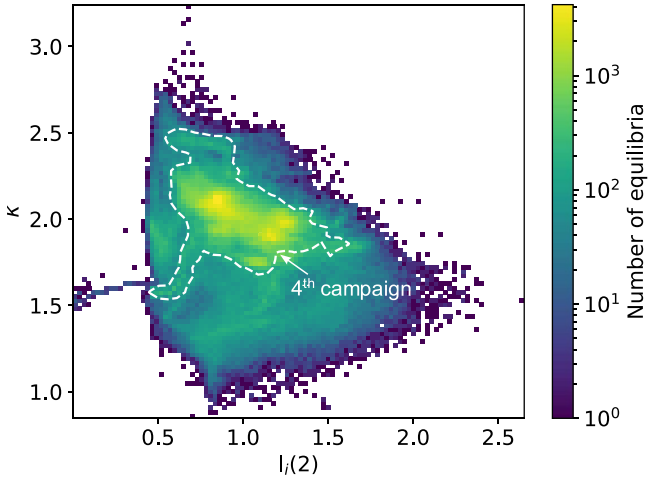

Figure 4. Operating space of MAST Upgrade to date, in terms of internal inductance and elongation from equilibrium reconstructions constrained by external magnetic flux measurements. The operating space in the most recent 4th physics campaign is highlighted, showing an expansion of the operating space toward higher elongation.

a conventional divertor configuration early in the pulse, from ∼40 ms after breakdown to reduce the influx of impurities from the inner wall during the limiter phase. The plasma is strongly shaped, with elongation $\kappa \sim 2.7$ during the ramp-up phase, reducing to 2.4–2.5 in the plasma current flat-top. The FreeGSNKE free-boundary equilibrium modelling code [13] was used to guide the development of the plasma current ramp-up phase and calculate equilibrium shape controllers. Strong shaping, coupled with early neutral beam injection, facilitates the formation of a hollow current profile and high q_0. For example, $q_0 \sim 2.0$ at 0.2 s in a typical high confinement scenario compared with 0.4 s in the high q_0 scenario. However, a hollow current profile forms in the high q_0 scenario that results in a strongly reverse shear q profile, which in turn can result in internal reconnection events when on-axis and off-axis neutral beam injection is applied. These internal reconnection events result in significantly reduced q_0 and can terminate the pulse if they are of sufficiently large amplitude. These reconnection events were avoided by increasing gas fuelling, which in turn reduces the temperature profile.

The development of alternative divertor configurations was facilitated by use of a new Tokamak Exhaust Designer tool [14]. It represents the flux from the poloidal field coils used to shape the plasma in terms of spherical harmonics, which significantly accelerates the calculations of the coil currents required to produce a given divertor configuration whilst preserving the shape of the plasma core, compared with equivalent calculations performed using typical free-boundary equilibrium codes. It can flexibly accommodate multiple constraints provided by the user, including limits on the allowable coil currents, position of the separatrix and isoflux surfaces, poloidal flux expansion and radial and vertical magnetic field components, including the position of null points. The output from the Tokamak Exhaust Designer has been used to calculate shape controllers to form a specified divertor configuration, under feedback or feedforward control.

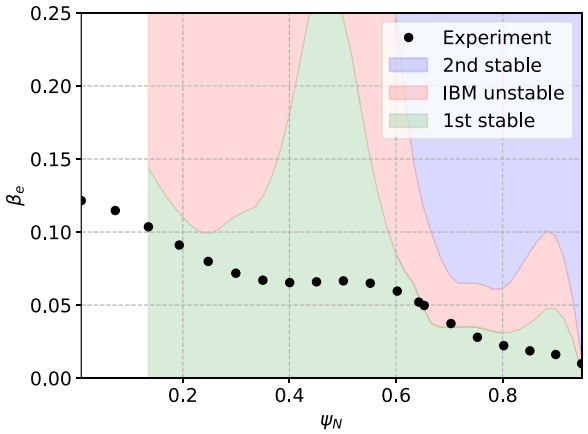

Figure 5. A profile of electron beta, β_e, from shot 48 657 at 0.6s. The parts of the profile that are stable to ideal ballooning modes (IBM, white), unstable (red) and in the 1st and 2nd stable regions (green and blue respectively) are highlighted.

3. Thermal confinement

A significant advantage of low aspect ratio devices is their ability to access high β (defined as the ratio of the plasma pressure and the pressure exerted by the confining magnetic field), offering a potentially economically attractive route to fusion energy production [4]. Predicting energy confinement in high β conditions with gyrokinetic models is challenging, as the electrostatic ion and electron temperature gradient driven modes that can govern confinement at low β can be replaced by electromagnetic instabilities such as microtearing and KBMs [15, 16]. Studies on MAST Upgrade have concentrated on accessing high β conditions and characterising turbulent transport to facilitate comparison with predictive simulations. For example, simulations of turbulent transport in the STEP device [17] predict strong turbulent heat fluxes over a range of β_e (defined as the ratio of the electron thermal pressure and the pressure exerted by the confining magnetic field) before reducing to more moderate values at higher β_e. The transition to the regime with moderate heat fluxes at higher β_e occurs due to the stabilisation of KBM-like modes, which is connected to the ideal ballooning mode (IBM). In a high β experiment performed on MAST Upgrade, shown in figure 5, it is demonstrated that part of the β_e profile lies on the ideal ballooning stability boundary where high heat fluxes would be expected in STEP-like conditions. It is posited that MAST Upgrade can access these conditions due to the strong toroidal flows and flow shear, present in current experiments due to strong torque injection from the neutral beams. The absence of strong flow shear would result in values of β_e unstable to the IBM to be inaccessible. A central aim of future experiments on MAST Upgrade will be to explore the roles of rotation and rotation shear on transport and confinement and their dependence on β_e to test these predictions.

The impact of stochastic magnetic field on electron heat transport in MAST and MAST Upgrade has been investigated over a range of collisionality. The physics guided Rechester–Rosenbluth (RR) model is used to describe the stochastic field contribution to electron heat transport, and to

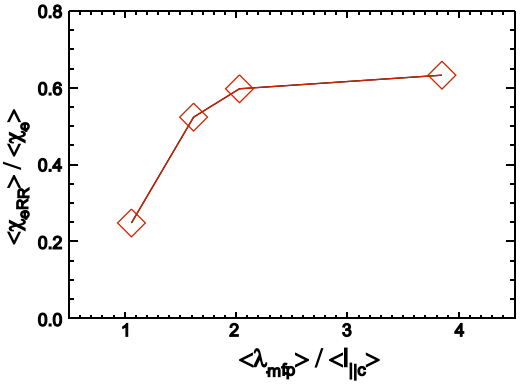

Figure 6. Ratio of the stochastic $<\chi_{eRR}>$ to total $<\chi_e>$ radial heat diffusion coefficients as a function of the ratio ion–electron collision mean free path λ_{mfp} to a characteristic length scale along the magnetic field $l_{||c}$.

supplement TGLF reduced model predictions of the transport from electrostatic turbulence. In the framework of the transport, results show a trend for which the importance of the stochasticity with respect to the other electrostatic/electromagnetic instabilities is established as a function of two important parameters represented by the mean free path for ion–electron collisions, λ_{mfp}, and a characteristic length scale $l_{||c}$ along the magnetic field direction [18]. Figure 6 shows the ratio between the average of stochastic diffusion coefficient $\langle\chi_{eRR}\rangle$ and the total diffusion coefficient $\langle\chi_e\rangle$ as a function of the ratio $\langle\lambda_{mfp}\rangle/\langle l_{||c}\rangle$. The average has been performed in the central radial region $r/a = [0.45, 0.75]$. A similar trend has been obtained by averaging diffusion coefficients on the complete radial domain until boundary conditions fixed at $r/a = 0.9$. It emerges that by moving from a more collisional regime in which $\langle\lambda_{mfp}\rangle \approx \langle l_{||c}\rangle$ towards to a collisionless regime in which $\langle\lambda_{mfp}\rangle \gg \langle l_{||c}\rangle$ the importance of stochastic transport increases. This suggests it may be possible to quantify the role of stochasticity in the different scenarios in tokamaks, and in particular in STs.

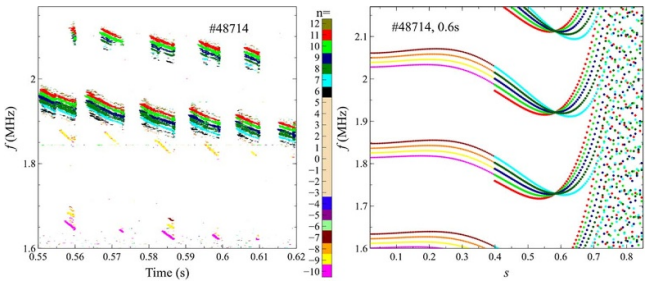

Figure 7. Left: measured frequencies and toroidal mode numbers of modes in the MHz range in pulse number 48 714. Right: global Alfvén continua calculated for this pulse at t = 0.6 s, Reproduced from [20]. © 2024 The Author(s). Published by IOP Publishing Ltd on behalf of the IAEA. CC BY 4.0.

4. Fast ion confinement

The confinement of energetic particles due to external heating in current devices and fusion reactions in future devices is critical for efficient plasma heating and current drive and to avoid excessive wall loads from lost fast ions. Modes with frequencies typically ranging from 1 to 2 MHz (up to around half the on-axis ion cyclotron frequency) are excited in most MAST Upgrade pulses with either on-axis only or on-axis and off-axis neutral beams and have previously been shown to cause fast ion losses [19]. Analysis of these pulses has shown that the modes have frequencies lying close to extrema in the global Alfvén eigenmode (GAE) continuum (figure 7), and eigenmodes at these frequencies have been found using the MISHKA linear ideal MHD code [20]. It is concluded from this analysis that the observed modes are indeed GAEs rather than compressional Alfvén eigenmodes (CAEs).

The appearance of these modes in the ion cyclotron range has motivated work to extend the linear theory of wave-particle interactions to modes of arbitrary frequency [21]. This study indicates that the resonance maps, and hence the expected fast ion losses, associated with GAEs and CAEs in general differ, suggesting that fast ion loss measurements could provide an additional means of distinguishing the two types of mode.

Charge-exchange (CX) with slow edge neutrals is a significant cause of fast ion losses in MAST Upgrade, particularly those originating from the off-axis beam, and an accurate description of this process is needed for fully quantitative modelling of plasma performance. To this end, dedicated experiments have been performed using both high-(HFS) and low-field side (LFS) gas fuelling to study CX losses of fast ions [22]. In these pulses a resistive bolometer normally used to record radiation losses was repurposed as a fast neutral diagnostic. The orbit-following ASCOT code, which can model neutralisation and reionisation of the fast ions, was used to simulate the fast neutral power load on the bolometer. In the case of HFS fuelling, a comparison between measured and simulated bolometer loads led to the conclusion that around 10% of the off-axis beam power was lost due to CX. For LFS fuelling, the comparison is complicated by toroidal asymmetries in the neutral density distribution, but it is clear that the CX losses are much higher in this case, up to about 50% of the off-axis beam power.

The first measurements of fusion protons have been obtained using a diamond detector that is more resilient to the environment of a fusion device, less sensitive to temperature variations than conventional silicon detectors, and offers improved reliability [23]. Considering these findings, an Upgraded proton detector has been developed that only contains diamond-based detectors. Measurements of fast ion losses with a Fast Ion Loss Detector have been tested against ASCOT simulations, to enable studies of the interaction of MHD instabilities on fast ion confinement, including type-III ELMs that result in a 25%–30% enhancement of fast ion losses from passing orbits [24].

5. MHD stability and disruptions

Studies of MHD stability on MAST Upgrade have concentrated on understanding and avoiding performance-limiting modes towards improving confinement of thermal and energetic species. As mentioned in section 2, $m/n = 2/1$ modes are commonly observed in neutral beam heated H-mode plasmas and can result in significant degradation of confinement of thermal and fast ions. A summary of a typical pulse exhibiting 2/1 mode activity is shown in figure 8. The appearance of the mode typically coincides with a strong deceleration of the toroidal rotation at the magnetic axis, matching the rotation velocity at the $q = 2$ flux surface later in the pulse. Once the rotation profiles have stabilised, the stored energy and the stored energy normalised to the ITER IPB98y,2 scaling ($H_{98y,2}$) [25] can decrease by up to 40% and the neutron rate (not shown) by up to 50%. The onset conditions for 2/1 instabilities on MAST Upgrade are similar to those observed in the DIII-D ITER baseline scenario [26], where the $q = 2$ flux surface is in close proximity to a local minimum in the toroidal current density profile (e.g. where $\mathrm{d}J_\phi/\mathrm{d}\psi_N = 0$). Experiments have been performed to modify the toroidal current density profile to postpone or avoid the onset of 2/1 modes, including applying vertical shifts and oscillations to the plasma to modify the profile of the neutral beam driven current and avoiding or delaying the L–H transition with gas fuelling from the LFS [27] to modify the edge bootstrap current. These techniques have not robustly avoided the onset of these modes, but can temporarily disrupt the 2/1 mode after it appears, resulting in a transient $\sim$15% increase in β_N before the 2/1 mode is re-established. As mentioned in section 2, the onset of 2/1 modes can be postponed via developing plasma scenarios optimised to produce an elevated q profile, in particular maximising elongation in the plasma current ramp-up and flat-top phases.

Understanding and predicting the evolution of the equilibrium q profile is an important goal of scenario modelling, due to its strong role in governing stability and confinement. Experiments performed with only on- or off-axis neutral beam heating can result in a sawtoothing phase. However, combined on- and off-axis neutral beam injection can facilitate access to a 'flux pumping' regime where $q_0 \sim 1$ in the absence of sawteeth [28], in contradiction to neoclassical current diffusion models that predict q_0 drops monotonically below 1 as the current density profile becomes more peaked (a typical

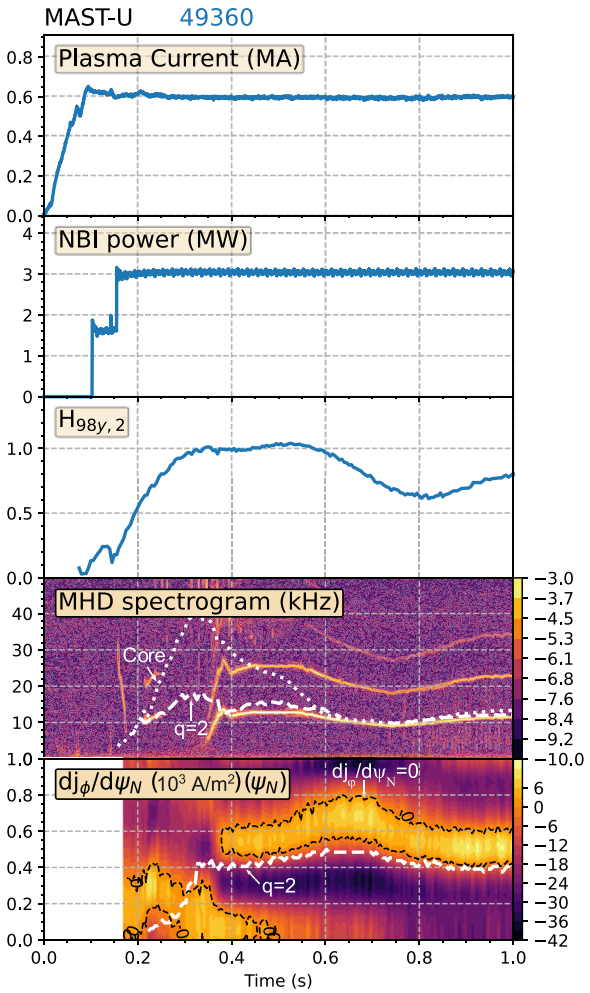

Figure 8. Summary of a typical NBI heated H-mode scenario. An MHD spectrogram (4th sub-figure) shows the toroidal rotation of the plasma core and q = 2 flux surface, showing a rapid deceleration of the core rotation after 400 ms, when the 2/1 mode appears. The appearance of this mode coincides with the q = 2 flux surface being in close proximity to a region where $dJ_\Phi/d\psi_N = 0$ (5th sub-figure, plotted as a function of normalised flux on the vertical axis).

MAST Upgrade pulse exhibiting flux pumping is shown in figure 9). Conditions to access the flux pumping regime in MAST Upgrade include high β_p, high q_{95} and weakly positive magnetic shear close to the magnetic axis. Flux pumping is observed in the presence of $m/n = 2/1$ modes that are ubiquitous in MAST Upgrade plasmas with strong auxiliary heating. It is not thought that long-lived 2/1 modes are prevalent in high-performance scenarios in STs in general, for example they were not commonly observed in NSTX experiments [29].

Operation at high elongation has been demonstrated to be a viable route to improved stability and performance in STs (e.g. [29].). However, ensuring robust vertical stability can be challenging, as the highest sustainable elongation is dependent on ensuring the radial current density profiles in the core are sufficiently broad (or, equivalently, the internal inductance is sufficiently low). This has motivated the development of advanced techniques to predict the radial current density profile, and in turn the vertical stability of strongly shaped plasmas within the DECAF framework [30] that can be applied to real-time

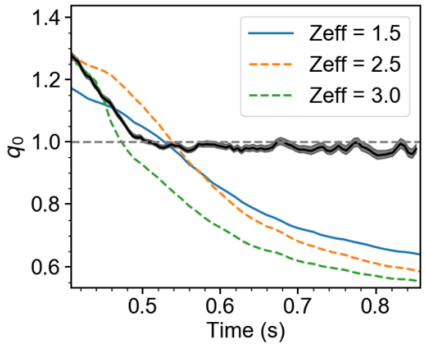

Figure 9. Comparison of the central safety factor, q_0, inferred from MSE constrained equilibrium reconstruction shown in black with estimates from TRANSP, using the NCLASS model of neoclassical current diffusion and different assumptions for the effective charge (Z_{eff}, blue, orange, green).

control systems. In preparation for the development of real-time disruption avoidance schemes, DECAF has been applied to the MAST Upgrade dataset to identify the chain of events that can result in a disruptive termination of the plasma [31].

6. Pedestal physics

The edge transport barrier that forms at the periphery of the confined plasma in the high confinement (H-mode) regime offers an attractive route to improved global energy confinement, however the steep pressure gradients can give rise to periodic ELM instabilities that transiently reduce confinement at the edge and elevate divertor power loads [32]. Studies on MAST Upgrade have concentrated on developing fundamental understanding of the processes that govern the height and width of the pedestal and avoiding ELMs both theoretically/computationally and experimentally whilst retaining the benefit of improved confinement in H-mode.

A new machine learning (ML) framework HIPED (height and width predictor for edge dynamics), has been designed for predicting and optimising pedestal and core performance in ST plasmas [33]. Using data from the third MAST-U campaign, HIPED demonstrated that the simple power-law relation between pedestal width and height typically used for conventional aspect ratio devices yield low accuracy for STs. When parameters like β_N, elongation, and Greenwald fraction were introduced, the predictive accuracy increased. HIPED also includes the possibility of multi-objective Pareto optimisation, which may allow experimentalists to systematically optimise outcomes by balancing competing goals, such as maximising plasma performance while avoiding ELMs, and identify the necessary control room parameters to achieve those outcomes. For example, discharges were identified from the third MAST-U campaign that lay on the optimised Pareto fronts with different weights on time between ELMs, Greenwald fraction, and β_N, and provided insights on plasma shaping and beam power used to achieve those conditions.

The tightly baffled divertor chambers and flexibility to vary the magnetic configuration within these divertors allows for

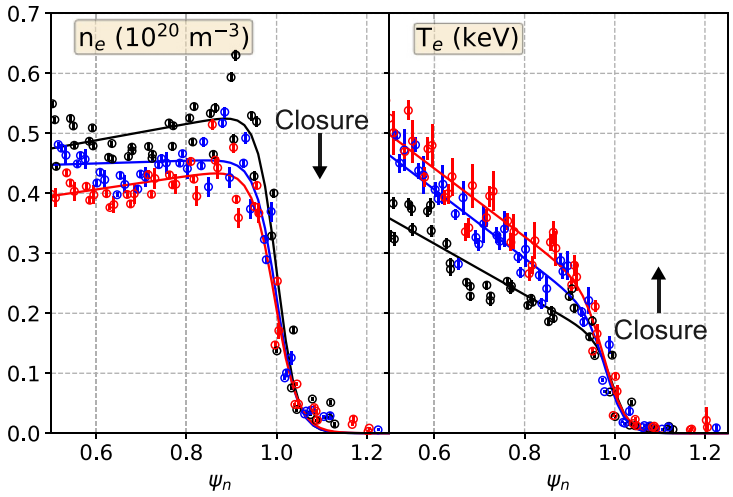

Figure 10. Radial profiles of electron density (left) and temperature (right) as the divertor closure and gas fuelling rate from the divertors are varied. In the most closed divertor configuration, shown in red, the temperature pedestal is highest and density is lowest. As closure decreases, in the blue profiles with a modest reduction in closure temperature decreases and density increases at constant pressure, but a stronger reduction in closure, shown in black, results in a reduction in the pedestal pressure profile.

detailed studies to understand the impact of fuel atoms and molecules interacting with the pedestal arising from the divertor, via either gas fuelling from the divertor or varying the position of the divertor strike point. Initial results from these studies are shown in figure 10, showing that increasing gas fuelling from the divertors or decreasing the divertor closure reduce the electron temperature at the pedestal top and elevate the pedestal density profile.

Recent experiments have successfully demonstrated access to small ELM (i.e. type-II ELMs or the quasi-continuous exhaust regime [34]) or stationary ELM-free pedestal regimes as a means of retaining the improved confinement of the H-mode pedestal whilst reducing (or eliminating) transient heat loads from ELMs. It has been demonstrated that strong shaping of the last closed flux surface, specifically a combination of either high squareness or high triangularity, can enable access to a small ELM regime, in qualitative agreement with theoretical predictions [35]. In these experiments, stability modelling performed with the ELITE code [36] indicate that the pedestal is limited by peeling-ballooning modes, predominantly by high-n ballooning modes. As the squareness of the last closed flux surface is increased, a transition from type-I to small ELMs occurs, and the stable region of the peeling-ballooning stability space decreases. Elevated D_α emission is observed in the main chamber, suggestive of increased ionisation of neutral particles in the main chamber, and Doppler backscattering measurements indicate there is evidence of increased radial particle transport across the pedestal. Access to a small ELM regime has also been demonstrated via strong gas fuelling from the main chamber, which induces a transition from a type-I ELMing regime. Equilibria with self-consistent bootstrap current are found to be unstable to $n = \infty$ ballooning modes near the separatrix in the small ELM regime and are stable to these modes in the type-I ELMing regime, consistent with studies performed on conventional aspect ratio devices [37].

The application of RMPs has successfully mitigated type-I ELMs using RMPs with toroidal mode number $n = 1$ with static [38], and more recently, toroidally rotating RMP fields. There has been no evidence of RMPs having a significant effect on ELMs by applying $n = 2$ perturbations, which is thought to be due to the interaction of the RMP with the $n = 2$ component of the intrinsic error field produced by small imperfections in the position, orientation or shape of the poloidal field coils used to shape the plasma. The resistive MHD code MARS-F has been extensively used to evaluate the possibility of directly measuring the plasma response in MAST-U, and particularly its variation as function of the applied poloidal spectrum, in order to guide the experimental validation of the predicted best RMP configuration for ELM suppression with $n = 2$ in double null topology [39]. The application of $n = 3$ RMPs has resulted in the successful suppression of ELMs for the first time in a ST. These experiments were performed in a lower single null topology (most STs operate close to a connected double null topology to minimise the heat flux to the relatively small inner divertors) and are summarised in figure 11. Comparison of otherwise similar pulses in the presence and absence of $n = 3$ RMPs show that their application results in a reduction in plasma density, from the centre of the plasma to the pedestal top and deceleration of the toroidal rotation, braking the rotation completely and the elimination of ELMs and an increase in the core ion temperature. Thermal energy confinement initially degrades by $\sim$10% after the RMPs are applied, followed by a recovery of later in the pulse. Thomson scattering measurements of the electron temperature profile indicate the presence of a pedestal when RMPs are applied.

Initial exploration of negative triangularity scenarios have been performed on MAST Upgrade for the first time in a low aspect ratio device [40], to enable detailed studies of the role of aspect ratio on confinement through comparison with negative triangularity experiments performed on higher aspect ratio

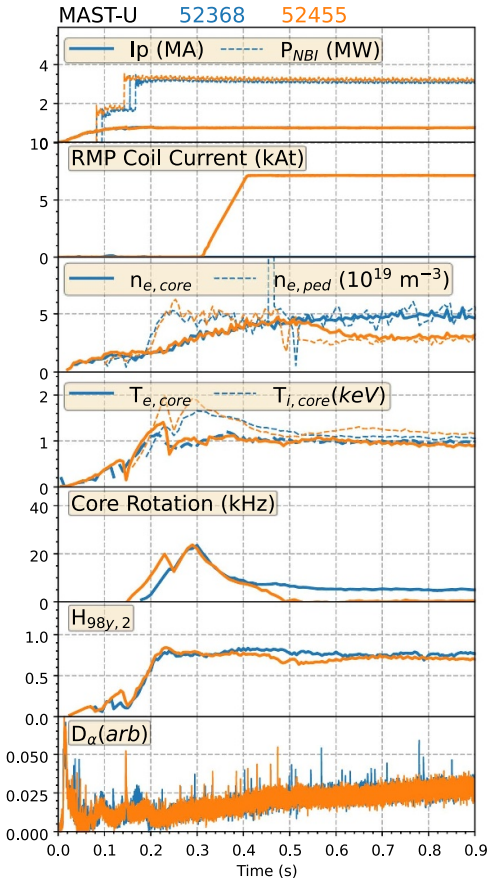

Figure 11. Demonstration of ELM suppression with n = 3 RMPs, comparing otherwise similar shots without (blue) and with (orange) RMPs applied. Top—plasma current (solid) and neutral beam heating power (dashed), 2nd from top—current in the RMP coils, 3rd from top—electron density in the plasma core (solid) and pedestal top (dashed), 4th from top—toroidal rotation at the magnetic axis, 5th from top—core energy confinement normalised to the ITER scaling [25], bottom—main chamber D_α emission.

devices such as TCV [41] and DIII-D [42]. A transition from type-III ELMing to an ELM-free regime was observed when the radial position of the primary X-points was swept outwards radially, finding that the transition occurs when the average triangularity (δ_{avg}) is below a critical value, $\delta_{avg} < -0.06$. As triangularity decreases, the electron temperature at the pedestal top also decreases, accompanied by a steady increase in the temperature in the core, thus maintaining $H_{98y,2}$ ($\sim$0.7) and β_N ($\sim$2) throughout the transition from type-III ELMing to ELM-free regimes. In this experiment, it was found that access to the second stability region for IBMs is closed 100 ms prior to the transition to an ELM-free regime, but experiments performed on higher aspect ratio devices report a transition to a quasi-stationary ELM-free regime coinciding with the closure of access to second stability.

Recent extended-MHD simulations with the M3D-C1 code have shown that plasma resistivity can play a role in destabilising peeling-ballooning modes in pulses with type-I ELMs on MAST Upgrade, but not on MAST [43]. This effect expands the unstable domain in the parameter space given by edge current density j and ballooning parameter α. It is seen that the magnetic shear in the pedestal correlates with the occurrence of resistive peeling-ballooning modes. These results enable the development of a high fidelity pedestal structure model for MAST Upgrade and other STs.

7. Plasma exhaust

Ensuring adequate power and particle exhaust in large, high power density tokamaks such as ITER and its successors remains a high priority for fusion research. MAST Upgrade has performed pioneering studies to improve understanding of power exhaust, including the physics of divertor detachment, and its integration with high-performance core and edge pedestals with tightly baffled, up-down symmetric divertor chambers that can support conventional and alternative divertor configurations. The operational space of MAST Upgrade has recently been expanded with an active cryopump in the lower divertor with a pumping speed of approximately 25 m^3 s^{-1}. Due to the cryopump being situated in the lower tightly baffled divertor chamber, its effect is localised to the lower divertor, as shown in figure 12. The ability to independently vary the plasma conditions and neutral density in each divertor, and the conditions in the main chamber from the divertors even in magnetic configurations close to connected double null, has greatly facilitated the integration of high-performance core and pedestals with detached divertors and independent control of the detachment state of each divertor, as discussed later in this section.

Studies of the impact of the cryopump and fuelling location on the separatrix density at the outer mid-plane have been performed in experiments and compared with SOLPS-ITER simulations [44]. In experiments with conventional and Super-X divertor configurations, with fuelling predominantly from the divertor chambers, a dependence of the separatrix density ($n_{e,sep}$) on divertor neutral pressure (P_n) is found $n_{e,sep} = 0.71 \times P_n^{0.3}$, in good agreement with simulations that yield a similar trend $n_{e,sep} = 0.69 \times P_n^{0.34}$, in qualitative agreement with trends observed on other devices [45, 46]. Conversely, experiments performed with fuelling from the main chamber, either from the high- or LFS, yield a higher exponent, $n_{e,sep} = 2.83 \times P_n^{0.62}$, which is notably different than the trend recovered from simulations $n_{e,sep} = 1.22 \times P_n^{0.83}$. These trends are independent of whether experiments employ a conventional or Super-X divertor configuration.

The Super-X divertor configuration [47] greatly facilitates access to the detached divertor regime [8, 48], such that the outer divertors are typically detached over the operating space of MAST Upgrade with minimal impact on the edge pedestal or plasma core. The plasma conditions in the divertor chambers in the Super-X configuration are typically low temperature ($T_e < 1$ eV) and low density ($n_e < 1 \times 10^{19}$ m^{-3}), where plasma–molecule interactions can result in significant dissipation of particles, momentum and energy from the plasma [48]. Measurements of D_2 Fulcher band emission in MAST Upgrade and TCV have been used to infer the rotational temperature of D_2 molecules [49]. These measurements show that as the separatrix density increases and the outer

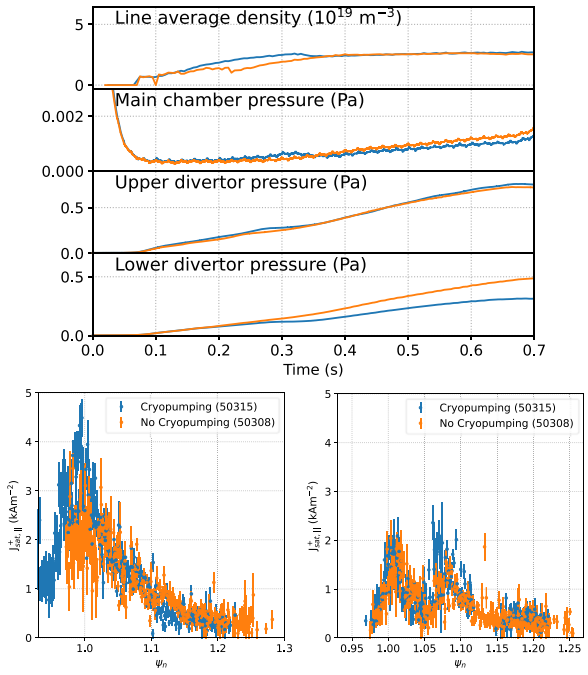

Figure 12. Top—summary of Ohmic heated experiments with (blue) and without (orange) an active lower divertor cryopump and a Super-X divertor configuration. Between 0.4 and 0.6 s, the line average density and neutral pressures in the upper divertor and main chamber are well matched, but the neutral pressure in the lower divertor is reduced by up to 30%. Bottom left—outer divertor ion saturation current density profiles from the lower divertor chamber between 0.4 and 0.6 s, showing that the ion flux increases in the presence of cryopumping, indicative of the divertor being less detached. Bottom right—outer divertor ion saturation current density profiles from the upper divertor, taken over the same period as for the lower divertor, which are unaffected by the lower divertor cryopump.

divertors are more deeply detached, the rotational temperature of D_2 molecules increases. This suggests that the plasma is transferring energy to D_2 molecules, which in turn can result in the formation of molecular ions that in turn react with the plasma via molecular activation ionisation, dissociation and recombination processes. However, the complexity of plasma–molecule interactions, with sufficient resolution to capture the ro-vibrational states of D_2, is challenging to incorporate in multi-fluid simulations such as SOLPS-ITER. Simulations have been performed with SOLPS-ITER of detachment onset and evolution in MAST Upgrade-like conditions in simplified geometry [50] with models of plasma–molecule interactions of increasing fidelity to estimate their impact on predictive simulations of present-day devices. Higher fidelity models of plasma–molecule interactions predict a ∼20% reduction in the upstream separatrix density required to detach the outer divertor leg, if the power entering the divertor leg is held constant, due to higher rates of molecular CX ($p + H_2 \rightarrow H + H_2^+$), thus elevating the density of molecular ions, leading to higher rates of molecular activated recombination and molecular activated dissociation.

In the double null topology, most of the power crossing the separatrix, P_{SOL}, flows to the outer divertors [51] where it can be effectively dissipated in the Super-*X* configuration. However, in the lower single null topology, a higher proportion of P_{SOL} flows to the relatively compact inner divertors in the Super-*X* configuration compared with a conventional divertor, which is consistent with analytic models [52]. As the heating power increases in future campaigns, and the electron temperature at the outer divertor targets increases, predictive SOLPS-ITER simulations with experimentally derived cross-field transport coefficients, suggest that the $E \times B$ drift enhances asymmetries between the upper and lower divertors will increase in a connected double null topology with Super-*X* outer divertor configurations [53].

Studies of core-edge-divertor integration were initially performed with the outer divertors in the Super-*X* configuration [8] and have recently been extended to study the *X*-point target [54]. These experiments show qualitatively similar behaviour as those performed in the Super-*X* configuration, indicating detached conditions at the outer divertor targets while having minimal impact on the edge pedestal or plasma core ($T_{e,core} \sim 1$ keV, $T_{e,ped} \sim 0.2$ keV, $H_{98y,2} \sim 0.7$–0.8, $\beta_N \sim 2.5$). Divertor Thomson scattering measurements indicate the electron temperature in the lower divertor is reduced in the *X*-point target configuration compared with an otherwise similar experiment with a Super-*X* configuration. Measurements of 2D electron density profiles via coherence imaging spectroscopy [55] in otherwise similar experiments with radially extended and *X*-point target divertor configurations (see figure 13), show that, while the peak electron density is similar, the radial width of the density profile is higher and the electron temperature is lower in the *X*-point target configuration. These effects arise due to a combination of higher poloidal flux expansion, and hence higher plasma volume in the divertor chamber, and the relatively long length scales of plasma–neutral interactions compared with the radial width of the divertor leg. In conditions where the outer divertor legs are more opaque to neutrals in future high power density tokamaks, these benefits are expected to be maintained if impurity seeding is used to ensure the ionisation front is close to, or upstream of the secondary *X*-point(s).

A substantial predicted benefit of alternative divertor configurations is improved controllability of divertor detachment [56], leveraging gradients in B (referred to here as 'total flux expansion', which in turn lead to gradients in the parallel heat flux) to passively stabilise the movement of the detachment front. These predictions were tested in system identification studies [57] using a sinusoidally varying fuelling rate from the divertor chambers to measure its impact on the detachment front, via multi-wavelength imaging of D_2 Fulcher band emission. Divertor configurations with the greatest total flux expansion exhibited the weakest response, facilitating real-time control, while divertor configurations with lower total flux expansion showed stronger response, which would be more challenging to control. The detachment state of each divertor can be varied independently when the plasma is close to a connected double null topology, such that the upper and lower outer divertors are connected via magnetic field lines. This behaviour is not commonly observed in present day experiments

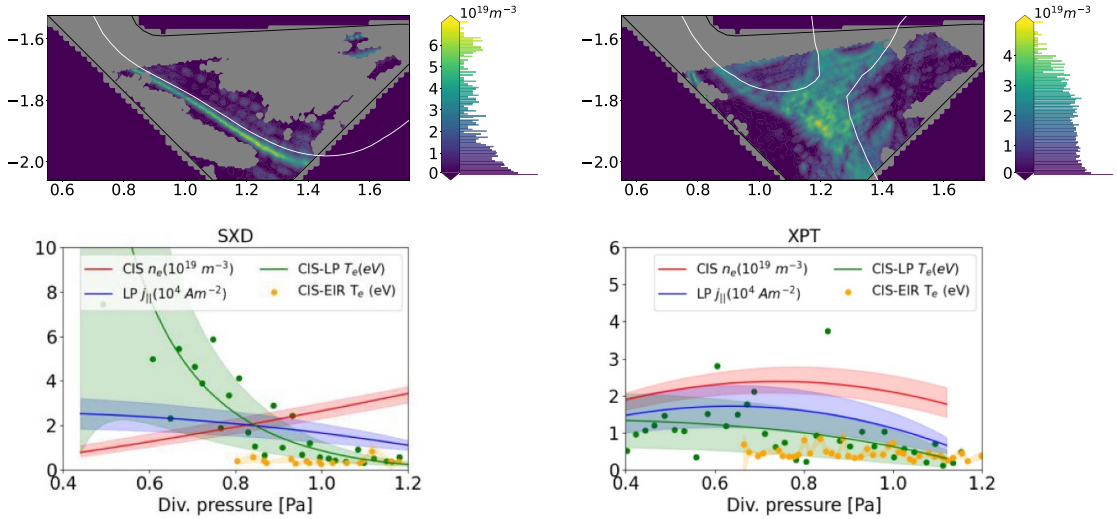

Figure 13. Left top—2D n_e profile in a Super-X divertor configuration with the equilibrium separatrix overlaid, left bottom—inferred electron density (red), temperature (green, yellow) and ion saturation current density (blue) profiles. Right top, bottom—profiles measured in the X-point target configuration, with the same layout as the plots on the left.

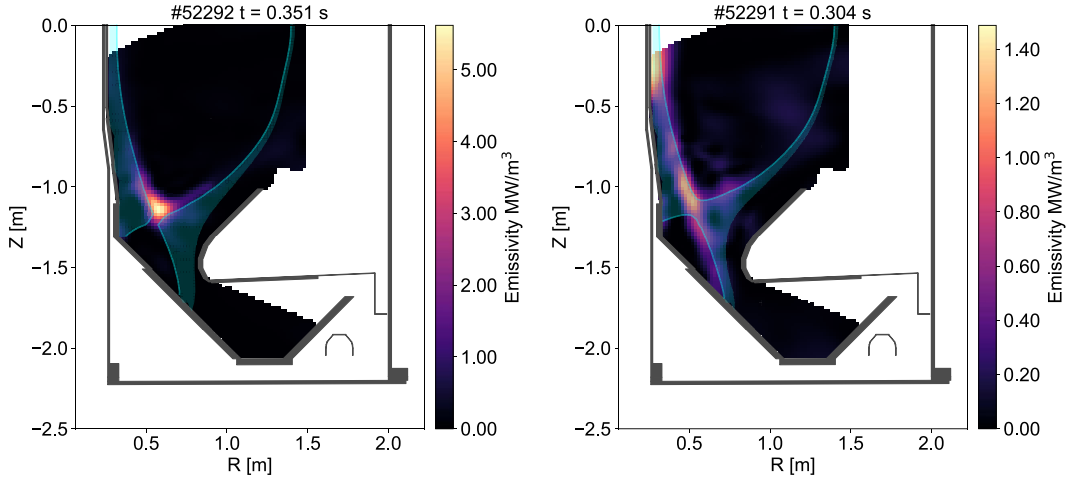

Figure 14. Emissivity of total radiated power from the lower half of MAST Upgrade in lower single null (left) and double null (right) X-point radiator regimes due to strong.

and manifests in MAST Upgrade due to the tightly baffled divertor chambers, and is expected in future devices that feature strong plasma plugging of the divertor entrance and tightly baffled divertors. Building on these system identification studies, real-time control of the detachment front position in the lower divertor chamber, inferred via real-time analysis of D_2 Fulcher band emission detected with the multi-wavelength imaging system, has been successfully demonstrated, using gas fuelling as the actuator. The real-time detachment control capability was applied to characterise the dynamics of divertor detachment and subsequent re-attachment, by increasing and decreasing fuelling rates respectively, showing that the timescales for re-attachment are shorter when the lower divertor cryopump is active. Coverage of the Multi-Wavelength Imaging systems and detachment control capabilities have been extended to the upper divertor chamber, allowing for simultaneous control of the detachment states of both divertors independently of each other and the density of the plasma core.

X-point radiator regimes (described in [58] and references therein) are an attractive power exhaust solution, where power is exhausted via a strongly radiating region within the confined plasma in the vicinity of the *X*-point through impurity seeding, as it can be readily implemented in existing tokamaks featuring divertors and has modest space requirements [59]. Initial development of *X*-point radiator regimes has progressed on MAST Upgrade using nitrogen impurity seeding under feedforward control to enhance radiation losses in the vicinity of the *X*-point(s) in lower single null and double null topologies in NBI heated H-mode experiments. The emissivity of radiation losses from the lower half of the device in the *X*-point radiator phases are shown in figure 14, showing strongly

localised losses in single null and a broader radiation distribution across the high-field side in double null. In both topologies, the onset of the *X*-point radiator regime resulted in a ∼20% reduction in energy confinement and approximately an order of magnitude reduction in the peak load to the outer divertor(s). Excessive radiation losses resulted in a H–L transition in single null and a transition to an ELM-free pedestal regime in double null.

8. Planned hardware enhancements and future programme

A programme of enhancements is underway to expand the operational space of MAST Upgrade towards more reactor-relevant conditions, including higher beta and lower collisionality in the plasma core and edge pedestal and to increase the heat flux entering the divertors to facilitate more stringent tests of the power handling capabilities of conventional and alternative divertor configurations. In 2027, two additional NBIs will be installed, both with a maximum injected power of 2.5 MW, one with a similar injection geometry as the existing off-axis beam, and the other will be intermediate between the existing on-axis and off-axis beams. This will double the neutral beam heating power available and provide significant flexibility to vary the fast ion pressure profile to avoid energetic particle instabilities driven by gradients in the fast ion pressure profile. In parallel, a 1.8 MW electron Bernstein wave (EBW) heating and current drive system is being developed [60], with injection frequencies of 28 GHz and 34.8 GHz to enable studies EBW mode conversion and current drive efficiency in on-axis and off-axis injection geometries, in support of the STEP physics mission. A high frequency pellet injector will be commissioned to enable studies of the impact of pellet fuelling on confinement and the development of power exhaust solutions that can accommodate modulations in plasma density due to pellet injection.

The future MAST Upgrade research programme will utilise these new capabilities to study thermal energy confinement at higher electron toroidal beta and the effects of toroidal rotation by varying the power injected from the neutral beam and EBW systems, and hence the net torque coupled to the plasma. Operation at higher heating power is expected to enable studies of MHD stability at values of β exceeding the no-wall stability limit [61], motivating the development of techniques to stabilise or control resistive wall modes. Studies of plasma exhaust and scenario integration will be extended to higher heat flux, enabling more detailed exploration of the onset of divertor detachment in alternative divertor configurations such as the Super-*X* and *X*-point target and more extensive use of impurity seeding to vary the degree of detachment of each divertor. As more diagnostics provide more real-time data output, the control capabilities of MAST Upgrade will expand to facilitate comparison of techniques to control plasma properties and the equilibrium in the main chamber and in the divertors. Initial studies of EBW heating and current drive will concentrate on power deposition and current drive to develop deeper understanding of EBW mode conversion and the role of Ohkawa and Fisch–Boozer current drive mechanisms and their dependences on plasma operating scenarios to test predictive models.

Acknowledgments

This work has been carried out within the framework of the EUROfusion Consortium, funded by the European Union via the Euratom Research and Training Programme (Grant Agreement No 101052200—EUROfusion) and from the EPSRC [Grant Number EP/W006839/1]. To obtain further information on the data and models underlying this paper please contact PublicationsManager@ukaea.uk. Views and opinions expressed are however those of the author(s) only and do not necessarily reflect those of the European Union or the European Commission. Neither the European Union nor the European Commission can be held responsible for them.

ORCID iDs

J.R. Harrison 0000-0003-2906-5097
H. Anand 0000-0002-9632-5680
Y. Andrew 0000-0003-0094-3503
L.C. Appel 0000-0001-9259-6240
A. Ash 0009-0006-9030-5984
F. Auriemma 0000-0002-1043-1563
P. Balazs 0000-0003-1227-7333
O. Bardsley 0000-0002-1525-675X
M. Barnes 0000-0002-0177-1689
J. Berkery 0000-0002-8062-3210
M. Bernert 0000-0003-1131-0867
W. Boeglin 0000-0001-9932-9161
C. Bowman 0000-0002-0813-2206
J. Bradley 0000-0002-8833-0180
D. Brida 0000-0002-8647-7058
P.K. Browning 0000-0002-7089-5562
D. Brunetti 0000-0001-8650-3271
L. Casali 0000-0003-2924-3674
M. Cecconello 0000-0002-2571-1920
B. Chapman-Oplopoiou 0000-0001-9879-2285
J. Clark 0000-0002-1578-2346
N. Crocker 0000-0003-2379-5814
I. Cziegler 0000-0003-1040-8918
Y. Damizia 0009-0006-0612-6300
E. Delabie 0000-0001-9834-874X
G.L. Derks 0000-0003-3420-0388
M. Dreval 0000-0003-0482-0981
M. Dunne 0000-0002-5259-9970
S. Elmore 0000-0003-0589-9513
M. Faitsch 0000-0002-9809-7490
F. Federici 0000-0002-9354-7309
N. Fedorczak 0000-0001-7123-7433
F. Felici 0000-0001-7585-376X
N. Ferraro 0000-0002-6348-7827
A.R. Field 0000-0003-0671-9668
R. Fitzpatrick 0000-0001-6237-9309
L. Frassinetti 0000-0002-9546-4494
S. Freethy 0000-0003-4535-565X

W. Fuller 0000-0001-9182-8572
S. Gabriellini 0000-0001-9488-5193
K. Gage 0000-0003-0262-416X
J. Galdon-Quiroga 0000-0002-7415-1894
M. Gambrioli 0009-0004-3801-6937
L. Garzotti 0000-0002-3796-9814
T.E. Gheorghiu 0000-0003-4254-9790
K.J. Gibson 0000-0001-9321-5091
E. Giovannozzi 0000-0002-0939-5120
M. Gorelenkova 0000-0001-8487-1396
J.P. Graves 0000-0002-7959-7959
V.H. Hall-Chen 0000-0001-6009-3649
C.J. Ham 0000-0001-9190-8310
S.S. Henderson 0000-0002-8886-1256
C. Hickling 0000-0003-0348-6926
B. Hnat 0000-0001-6498-2953
L. Howlett 0000-0001-8105-8180
A. Hudoba 0000-0002-8197-7977
J. Hughes 0000-0003-4802-4944
K. Imada 0000-0002-8128-2438
P. Jacquet 0000-0001-7919-1206
S. Kaye 0000-0002-2514-1163
Y.O. Kazakov 0000-0001-6316-5441
D. Keeling 0000-0002-3581-7788
D. Kennedy 0000-0001-7666-782X
H-T. Kim 0009-0008-2549-5624
D. King 0000-0001-5128-5083
A. Kirk 0000-0002-5746-6595
A. Kleiner 0000-0002-5800-8027
M. Knolker 0000-0002-8468-8767
M. Kochan 0009-0007-9616-5828
L. Kogan 0009-0002-9158-4920
B. Kool 0000-0002-1636-7400
M. Kotschenreuther 0000-0001-6327-877X
M. Lampert 0000-0002-8462-8799
K. Lawson 0000-0002-1251-6392
A.W. Leonard 0000-0001-9356-1074
B. Lipschultz 0000-0001-5968-3684
E. Litherland-Smith 0009-0000-0587-2930
Y.Q. Liu 0000-0002-8192-8411
B.A. Lomanowski 0000-0003-2226-2004
N. Lonigro 0000-0001-8581-0384
J. Lore 0000-0002-9192-465X
J. Lovell 0000-0001-9565-3466
T. Macwan 0000-0002-9767-0830
R. Maingi 0000-0003-1238-8121
S. Marsden 0009-0005-1175-7329
R. Maurizio 0000-0001-9896-6732
R. McAdams 0000-0001-8607-8201
G. McArdle 0000-0003-0888-0105
K. McClements 0000-0002-5162-509X
K. McKay 0000-0003-1822-7994
A. McLean 0000-0002-0697-4397
B.F. McMillan 0000-0003-1509-2940
F. Militello 0000-0002-8034-4756
D. Moiraf 0009-0006-0686-4979
R. Morales Gomes 0000-0003-0667-3356
D. Morbey 0000-0001-6207-9832
S. Mordijck 0000-0001-8537-4383
D. Moulton 0009-0001-8439-9551
S. Munaretto 0000-0003-1465-0971
O. Myatra 0000-0002-1469-2429
T.F. Neiser 0000-0002-8763-3016
A.O. Nelson 0000-0002-9612-1936
M.G. O'Mullane 0000-0002-2160-4546
H.J. Oliver 0000-0002-7302-085X
P. Ollus 0000-0003-2558-1457
J. Omotani 0000-0002-3156-8227
R. Osawa 0000-0002-8152-2323
N. Osborne 0000-0002-6079-9550
T. Osborne 0000-0003-2641-4597
R. Otin 0000-0002-3053-2695
F. Palermo 0000-0002-7524-3248
I. Paradela Pérez 0009-0003-4812-5136
J. Parisi 0000-0003-1328-7154
B.S. Patel 0000-0003-0121-1187
E. Pawelec 0000-0003-1333-6331
C. Paz-Soldan 0000-0001-5069-4934
L. Piron 0000-0002-7928-4661
C. Piron 0000-0002-4441-9781
G. Pucella 0000-0002-9923-2770
H. Reimerdes 0000-0002-9726-1519
T. Rhodes 0000-0002-8311-4892
J.F. Rivero-Rodriguez 0000-0001-5074-0267
D. Ryan 0000-0002-7735-3598
P. Ryan 0000-0002-7133-6156
S. Saarelma 0000-0002-6838-2194
S. Sabbagh 0000-0003-1077-8118
A. Salmi 0000-0002-3306-6335
O. Sauter 0000-0002-0099-6675
S. Sharapov 0000-0001-7006-4876
S.A. Silburn 0000-0002-3111-5113
J. Simpson 0000-0002-0083-9637
A. Sladkomedova 0000-0002-0012-9328
V.A. Soukhanovskii 0000-0001-5519-0145
D. Speirs 0000-0001-5705-6126
G. Staebler 0000-0002-1944-1733
J. Stobbs 0009-0000-0649-5698
T. Tala 0000-0002-6264-0797
C. Theiler 0000-0003-3926-1374
R.G.L. Vann 0000-0002-3105-2546
K. Verhaegh 0000-0002-0500-2764
C. Vincent 0000-0002-7227-409X
S. Wiesen 0000-0002-3696-5475
T.A. Wijkamp 0000-0003-3110-8682
H.R. Wilson 0000-0003-3333-7470
V. Zamkovska 0000-0001-8437-4576

References

[1] Harrison J.R. *et al* 2024 Overview of physics results from MAST Upgrade towards core-pedestal-exhaust integration *Nucl. Fusion* **64** 112017
[2] Berkery J.W. and Harrison J.R. 2025 A review of collaborative studies between the NSTX/-U and MAST/-U spherical tokamaks *Plasma Phys. Control. Fusion* **67** 053001

[3] Zohm H. *et al* 2013 On the physics guidelines for a tokamak DEMO *Nucl. Fusion* **53** 073019
[4] Meyer H. 2024 Plasma burn—Mind the gap *Phil. Trans. R. Soc. A* **382** 20230406
[5] Menard J.E. *et al* 2016 Fusion nuclear science facilities and pilot plants based on the spherical tokamak *Nucl. Fusion* **56** 106023
[6] Derks G.L. *et al* 2024 Development of real-time density feedback control on MAST-U in L-mode *Fusion Eng. Des.* **202** 114387
[7] Di Grazia L.E., Vincent C., Mattei M., Felici F., Kogan L. and Mele A. 2025 Iterative learning optimization and control of MAST-U breakdown and early ramp-up scenarios *Optim. Eng.* **2025** 1–22
[8] Harrison J.R., Bowman C., Clark J.G., Kirk A., Lovell J., Patel B.S., Ryan P., Scannell R., Thornton A.J. and Verhaegh K. 2024 Benefits of the Super-X divertor configuration for scenario integration on MAST Upgrade *Plasma Phys. Control. Fusion* **66** 065019
[9] Kim H.-T. *et al* 2022 Development of full electromagnetic plasma burn-through model and validation in MAST *Nucl. Fusion* **62** 126012
[10] Anand H. *et al* 2024 Real-time plasma equilibrium reconstruction and shape control for the MAST Upgrade tokamak *Nucl. Fusion* **64** 086051
[11] Lvovskiy A. *et al* 2025 Framework for assessment of magnetic equilibrium controller performance on the MAST Upgrade spherical tokamak *Plasma Phys. Control. Fusion* **67** 075003
[12] Parisi J.F. *et al* 2024 Kinetic-ballooning-limited pedestals in spherical tokamak plasmas *Nucl. Fusion* **64** 054002
[13] Amorisco N.C., Agnello A., Holt G., Mars M., Buchanan J. and Pamela S. 2024 FreeGSNKE: a Python-based dynamic free-boundary toroidal plasma equilibrium solver *Phys. Plasmas* **31** 42517
[14] Bardsley O.P., Baker J.L. and Vincent C. 2024 Decoupled magnetic control of spherical tokamak divertors via vacuum harmonic constraints *Plasma Phys. Control. Fusion* **66** 055006
[15] Kaye S.M., Connor J.W. and Roach C.M. 2021 Thermal confinement and transport in spherical tokamaks: a review *Plasma Phys. Control. Fusion* **63** 123001
[16] Kennedy D., Giacomin M., Casson F.J., Dickinson D., Hornsby W.A., Patel B.S. and Roach C.M. 2023 Electromagnetic gyrokinetic instabilities in STEP *Nucl. Fusion* **63** 126061
[17] Kennedy D. 2025 A tale of two (VISCO) cities electromagnetic turbulence and transport bifurcations: implications for next-generation fusion power plants *Nucl. Fusion* submitted
[18] Palermo F., Casson F.J., Koechl F., Chulu-Chinn N., McMillan B.F., Garzotti L., Angioni C. and Roach C.M. 2025 Validation and predictions of reduced models for stochastic electron transport in MAST and MAST-U *Plasma Phys. Control. Fusion* **67** 065004
[19] Rivero-Rodríguez J.F. *et al* 2024 Overview of fast particle experiments in the first MAST Upgrade experimental campaigns *Nucl. Fusion* **64** 086025
[20] Dreval M.B., Oliver H.J.C., Sharapov S.E., Rivero-Rodriguez J.F., Fitzgerald M., Michael C., Ochoukov R., Velarde L., Cecconello M. and Ryan D. 2025 Observation of bi-directional global Alfvén eigenmodes in the MAST-U tokamak *Nucl. Fusion* **65** 016043
[21] Fitzgerald M. and Breizman B.N. 2025 Solution of the linear wave-particle kinetic equation for global modes of arbitrary frequency in a tokamak *Fundam. Plasma Phys.* **13** 100084
[22] Ollus P., Kurki-Suonio T., Lovell J., McClements K.G., Michael C.A. and Snicker A. 2025 Charge-exchange losses of beam ions in MAST Upgrade: experiments and modelling *Plasma Phys. Control. Fusion* **67** 055039
[23] Aboutaleb A., Allan S.Y., Boeglin W.U., Cecconello M., Jackson A., McClements K.G. and Parr E. 2024 First measurements of energetic protons in Mega Amp Spherical Tokamak Upgrade (MAST-U) *Rev. Sci. Instrum.* **95** 83522
[24] Velarde L. *et al* 2025 Velocity-space analysis of fast-ion losses measured in MAST-U using a high-speed camera in the FILD detector *Plasma Phys. Control. Fusion* **67** 015024
[25] Kardaun O.J.W.F. 2002 On estimating the epistemic probability of realizing Q = Pfus/Paux larger than a specified lower bound in ITER *Nucl. Fusion* **42** 307
[26] Turco F., Luce T.C., Boyes W., Hanson J.M. and Hyatt A.W. 2024 Modelling and experiment to stabilize disruptive tearing modes in the ITER baseline scenario in DIII-D *Nucl. Fusion* **64** 076048
[27] Valovic M. *et al* 2002 Inboard gas puffing and behaviour of H-mode edge parameters in COMPASS-D *Plasma Phys. Control. Fusion* **44** 314
[28] Blackmore S. 2025 Investigation of the magnetic flux pumping effect in MAST Upgrade
[29] Gerhardt S.P. *et al* 2011 Recent progress towards an advanced spherical torus operating point in NSTX *Nucl. Fusion* **51** 073031
[30] Tobin M. *et al* 2024 Vertical instability forecasting and controllability assessment of multi-device tokamak plasmas in DECAF with data-driven optimization *Plasma Phys. Control. Fusion* **66** 105020
[31] Zamkovska V. *et al* 2024 DECAF cross-device characterization of tokamak disruptions indicated by abnormalities in plasma vertical position and current *Nucl. Fusion* **64** 066030
[32] Eich T., Sieglin B., Thornton A.J., Faitsch M., Kirk A., Herrmann A. and Suttrop W. 2017 ELM divertor peak energy fluence scaling to ITER with data from JET, MAST and ASDEX Upgrade *Nucl. Mater. Energy* **12** 84–90
[33] Parisi J.F. *et al* 2025 HIPED: machine learning framework for spherical tokamak pedestal prediction and optimization *Nucl. Fusion* **66** 026034
[34] Fenstermacher M.E. *et al* 2025 Progress in pedestal and edge physics: chapter 3 of the special issue: on the path to tokamak burning plasma operation *Nucl. Fusion* **65** 053001
[35] Parisi J.F. *et al* 2025 Prediction of ELM-free operation in spherical tokamaks with high plasma squareness (available at: https://arxiv.org/pdf/2505.02727) (Accessed 17 November 2025)
[36] Wilson H.R. and Cowley S.C. 2004 Theory for explosive ideal magnetohydrodynamic instabilities in plasmas *Phys. Rev. Lett.* **92** 175006
[37] Dunne M., Faitsch M., Radovanovic L. and Wolfrum E. 2024 Quasi-continuous exhaust operational space *Nucl. Fusion* **64** 124003
[38] Ryan D.A. *et al* 2024 First observation of RMP ELM mitigation on MAST Upgrade *Plasma Phys. Control. Fusion* **66** 105003
[39] Munaretto S., Liu Y.Q., Ryan D.A., Hao G.Z., Berkery J.W., Blackmore S. and Kogan L. 2024 Chasing the multi-modal plasma response in MAST-U *Plasma Phys. Control. Fusion* **66** 065023
[40] Nelson A.O. *et al* 2024 First access to ELM-free negative triangularity at low aspect ratio *Nucl. Fusion* **64** 124004
[41] Coda S. *et al* 2022 Enhanced confinement in diverted negative-triangularity L-mode plasmas in TCV *Plasma Phys. Control. Fusion* **64** 014004
[42] Thome K.E. *et al* 2024 Overview of results from the 2023 DIII-D negative triangularity campaign *Plasma Phys. Control. Fusion* **66** 105018
[43] Kleiner A., Imada K., Ebrahimi F., Ferraro N.M., Haskey S.R., Kogan L. and Pankin A. 2025 A study of resistive peeling–ballooning modes across spherical tokamaks *Plasma Phys. Control. Fusion* **67** 085026

[44] Xia Q. 2025 Cryopump and fuelling location impacts on upstream density and detachment on MAST-U *Nucl. Fusion* submitted
[45] Kallenbach A., Sun H.J., Eich T., Carralero D., Hobirk J., Scarabosio A. and Siccinio M. 2018 Parameter dependences of the separatrix density in nitrogen seeded ASDEX Upgrade H-mode discharges *Plasma Phys. Control. Fusion* **60** 045006
[46] Frassinetti L. *et al* 2021 Role of the separatrix density in the pedestal performance in deuterium low triangularity JET-ILW plasmas and comparison with JET-C *Nucl. Fusion* **61** 126054
[47] Valanju P.M., Kotschenreuther M., Mahajan S.M. and Canik J. 2009 Super-X divertors and high power density fusion devices *Phys. Plasmas* **16** 56110
[48] Verhaegh K. *et al* 2023 Spectroscopic investigations of detachment on the MAST Upgrade Super-X divertor *Nucl. Fusion* **63** 016014
[49] Osborne N., Verhaegh K., Bowden M.D., Wijkamp T., Lonigro N., Ryan P., Pawelec E., Lipschultz B., Soukhanovskii V. and van den Biggelaar T. 2024 Initial Fulcher band observations from high resolution spectroscopy in the MAST-U divertor *Plasma Phys. Control. Fusion* **66** 025008
[50] Bryant J., McKay K., Harrison J.R., Moulton D., Verhaegh K., Cowley C., Bergmayr R.C., Fantz U. and Wünderlich D. 2025 Impact of Yacora evaluated molecular effective rate coefficients on detached SOLPS-ITER simulations *Nucl. Fusion* **65** 036025
[51] Lovell J., Henderson S.S., Stobbs J.M., Kirk A., Federici F., Patel B.S., Ryan P.J., Harrison J.R., Lomanowski B.A. and Lore J.D. 2024 Experimental investigation of steady state power balance in double null and single null H mode plasmas in MAST Upgrade *Nucl. Mater. Energy* **41** 101779
[52] Maurizio R. *et al* 2019 Conduction-based model of the scrape-off layer power sharing between inner and outer divertor in diverted low-density tokamak plasmas *Nucl. Mater. Energy* **19** 372–7
[53] Pérez I.P., Lomanowski B., Lore J.D., Lovell J. and Moulton D. 2025 Power balance and divertor asymmetries in the Super-X divertors of MAST-U using SOLPS-ITER *Nucl. Fusion* **65** 066026
[54] LaBombard B. *et al* 2015 ADX: a high field, high power density, advanced divertor and RF tokamak *Nucl. Fusion* **55** 053020
[55] Lonigro N. *et al* 2025 First 2D electron density measurements using multi-delay coherence imaging spectroscopy in the MAST-U Super-X divertor *Plasma Phys. Control. Fusion* **67** 035003
[56] Lipschultz B., Parra F.I. and Hutchinson I.H. 2016 Sensitivity of detachment extent to magnetic configuration and external parameters *Nucl. Fusion* **56** 056007
[57] Kool B. *et al* 2025 Demonstration of Super-X divertor exhaust control for transient heat load management in compact fusion reactors *Nat. Energy* **10** 1116–31
[58] Stroth U., Bernert M., Brida D., Cavedon M., Dux R., Huett E., Lunt T., Pan O. and Wischmeier M. (the ASDEX Upgrade Team) 2022 Model for access and stability of the X-point radiator and the threshold for marfes in tokamak plasmas *Nucl. Fusion* **62** 076008
[59] Lunt T., Bernert M., Brida D., David P., Faitsch M., Pan O., Stieglitz D., Stroth U. and Redl A. 2023 Compact radiative divertor experiments at ASDEX Upgrade and their consequences for a reactor *Phys. Rev. Lett.* **130** 145102
[60] Jacquet P. 2025 The construction and commissioning of the electron Bernstein wave heating and current-drive system for MAST-U *Nucl. Fusion* submitted
[61] Berkery J.W., Xia G., Sabbagh S.A., Bialek J.M., Wang Z.R., Ham C.J., Thornton A. and Liu Y.Q. 2020 Projected global stability of high beta MAST-U spherical tokamak plasmas *Plasma Phys. Control. Fusion* **62** 085007